

1 Unilaterally Constrained Motion 2 of a Curved Surgical Tool

3 Bassem Dahroug* , Brahim Tamadazte and Nicolas
4 Andreff

Q1

5 AS2M Department, FEMTO-ST Institute, Univ. Bourgogne Franche-Comté/CNRS, 24 Rue Alain
6 Savary, 25000 Besançon, France

Q2

7 E-mails: brahim.tamadazte@femto-st.fr, nicolas.andreff@femto-st.fr

8 (Accepted November 1, 2019)

9 SUMMARY

10 Constrained motion is essential for varying robotics tasks, especially in surgical robotics, for instance,
11 the case of minimally invasive interventions. This article proposes generic formulations of the classi-
12 cal bilateral constrained motion (i.e., when the incision hole has almost the same diameter as that of
13 the tool) as well as unilaterally constrained motion (i.e., when the hole incision has a larger diameter
14 compared to the tool diameter). One of the latter constraints is combined with another surgical task
15 such as incision/ablation or suturing a wound (modeled here by 3D geometric paths). The developed
16 control methods based on the hierarchical task approach are able to manage simultaneously the con-
17 strained motion (depending on the configuration case, i.e., bilateral or unilateral constraint) and a 3D
18 path following. In addition, the proposed methods can operate with both straight or curved surgical
19 tools. The proposed methods were successfully validated in various scenarios. Foremost, a simula-
20 tion framework was proposed to access the performances of each proposed controller. Thereafter,
21 several experimental validations were carried out. Both the simulation and experimental results have
22 demonstrated the relevance of the proposed approach, as well as promising performances in terms of
23 behavior as well as accuracy.

Q3

24 KEYWORDS: Constrained motion modeling; Bilateral and unilateral constraints; 3D path follow-
25 ing; Hierarchical tasks; Medical robotics.

26 1. Introduction

27 Minimally invasive surgical (MIS) robotic systems enter into the human body either from a natural
28 orifice (anal cavity, mouth, urethra, nasal cavity, etc.) or from an artificial (i.e., created) hole. In both
29 cases, the robotic tool must avoid damaging the incision walls and the anatomical structures within
30 the patient's body. Most of the medical purposes (e.g., laparoscopic^{1,2} or eye^{3,4} surgeries) consider
31 that the incision hole diameter and that of the surgical tool are nearly equal.

32 Throughout this case, the tool linear motion is restricted locally along two axes of the incision
33 frame (e.g., the x -axis and z -axis as shown in Fig. 1(a)). Hence, the center point of the incision hole
34 (or the trocar center point) should constantly lay on the tool center line. The resulting constrained
35 motion is typically called *Remote Center of Motion* (RCM) (or *fulcrum effect*).^{5,6} Such constraints
36 are mathematically modeled with equality constraint equations, also known as bilateral constraints
37 in optimization theory.⁷

38 Nevertheless, bilateral constraints are excessively restrictive during other surgery types (e.g., in
39 the nose^{8,9} or the ear^{10–12}) where the orifice size is bigger than that of the tool. It implies that the

* This work has been supported by the ANR μ RoCS Project (ANR-17-CE19-0005-04).
Corresponding author. E-mail: bassem.dahroug@femto-st.fr

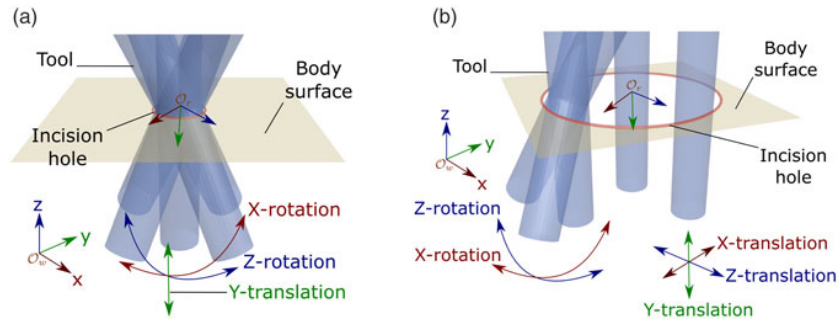


Fig. 1. A comparison between constrained motion: (a) RCM and (b) UCM.

40 orifice wall forms locally a cylinder around the instrument body. In this case, the tool is unconstrained
 41 within the hole before it hits the orifice wall (Fig. 1(b)). When the tool contacts the wall, its motion
 42 is constrained to slide along the wall contact point (i.e., performing the RCM movement at the contact
 43 point) to reach targets deeper inside the body. This motion is therefore restricted by inequality
 44 constraints and will be named within this paper as *Unilaterally Constrained Motion* (UCM).

45 A complex surgical task (e.g., suturing a wound, examining a region of interest, or excising patho-
 46 logical tissues) requires defining one of these constrained motions as a subtask. Indeed, this complex
 47 surgical task can be defined as a concatenation of several elementary subtasks, that is, a path follow-
 48 ing (representing an incision/ablation surgical gesture) under the RCM/UCM constraints. Setting up
 49 a hierarchy between these subtasks offers a solution to stack all of them. Thereby, the priority tech-
 50 nique¹³ based on the projection gradient method¹⁴ is applied for projecting a secondary task into the
 51 null space of the primary task. This task hierarchical management ensures to find out the secondary
 52 solution that does not generate conflict with the primary solution. This formalism was used to build
 53 a complex task from individual subtasks as in ref. [15].

54 Moreover, surgical tasks in confined spaces, for instance, the middle ear cavity or the superior part
 55 of the sinuses, are complex assignments. They impose the usage of the curved tools to (i) increase the
 56 surgeon's dexterity and (ii) allow reaching distal regions that cannot be accessed with conventional
 57 straight instruments. This makes it even harder to cope with both the clinical task and the anatomical
 58 constraints. Thereby, it is necessary to formulate a *generic solution* for handling also curved surgical
 59 tools under geometric (bilateral or unilateral) constraints.

60 Consequently, the article contributions provide a unified approach to manipulate either a straight or
 61 curved tool for following a user-defined 3D path under unilateral or bilateral anatomical constraints.
 62 In the remainder of this paper, Section 2 discusses the state of the art dealing with constrained motion
 63 control as well as the reasons why our proposed method goes beyond the current methods. Section 3
 64 recalls how a straight tool follows a reference path under bilateral constraints. After that, Section 4
 65 proposes the formulation of bilateral constraints with a curved tool, while Section 5 discusses the
 66 model of a curved tool that follows a path under unilateral constraints. The proposed methods were
 67 validated in both numerical (simulation) and experimental scenarios as discussed in Section 6 and 7,
 68 respectively.

69 2. Overview and Contributions

70 2.1. Overview

71 From a mathematical point of view, RCM is considered as a linear (respectively, nonlinear) equality
 72 system, where the system function must be equal to zero (i.e., $f(\mathbf{x}) \leq \mathbf{0}$ and $f(\mathbf{x}) \geq \mathbf{0} \Leftrightarrow f(\mathbf{x}) = \mathbf{0}$, as
 73 depicted in Fig. 2(a)). In opposition, UCM is considered as a linear (respectively, nonlinear) inequal-
 74 ity system, where the system function should be exclusively positive or negative (i.e., $f(\mathbf{x}) \leq \mathbf{0}$ xor
 75 $f(\mathbf{x}) \geq \mathbf{0}$, Fig. 2(b)).

76 RCM has been widely discussed in the literature from a mechanical viewpoint as, for instance, in
 77 refs. [5, 16]. Indeed, these works built a special kinematic structure in order to ensure the fulcrum
 78 effect constraints. The advantage of such a method is to physically impose the constrained motion
 79 the relatively easy formulation of the resulting control law. Despite that, a special structure does
 80 not provide enough flexibility to change the location of penetration point during the surgery. On

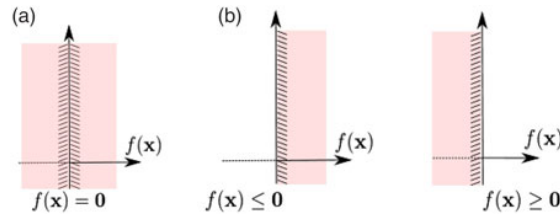


Fig. 2. A comparison from a mathematical viewpoint between (a) bilateral constraints and (b) unilateral constraints.

81 the opposition, a software controller can also achieve the required motion by guiding a general-
 82 purpose robot that is commercially present with a large range of models. The latter solution releases
 83 the mechanical constraints from the robot structure and adds the versatility of use thanks to the
 84 redundancy.

85 There are various methods reported in the literature for solving RCM by control, such as (i)
 86 extended Jacobian with quadratic optimization,¹⁷ (ii) gradient projection approach in closed-loop
 87 scheme,¹⁸ (iii) dual quaternion-based kinematic controller,¹⁹ and (iv) constrained Jacobian repre-
 88 sented with *Lie Algebra*.²⁰ These methods impose the bilateral constraints in the joint space (i.e.,
 89 onto the robot kinematic Jacobian matrix $\mathbf{J}(\mathbf{q})$) for restricting the kinematics to $\mathbf{v}_e = \mathbf{J}_{con}(\mathbf{q})\dot{\mathbf{q}}$. The
 90 new constrained Jacobian matrix $\mathbf{J}_{con} \in \mathbb{R}^{6 \times n}$ is a transformation that maps the joints velocities
 91 $\dot{\mathbf{q}} \in \mathbb{R}^{n \times 1}$ into the end-effector twist vector $\mathbf{v}_e \in se(3)$. However, this formulation requires an accurate
 92 knowledge of the robot kinematic model in order to implement the control law.

93 Furthermore, other authors have been proposed different approaches to formulate the constrained
 94 motion as (i) analytical solution based on trocar modeling with Euler angles representation,²¹ (ii)
 95 geometric solution-based heuristic search,²² and (iii) geometric constraint with stereo visual servo-
 96 ing.¹ These methods are more generic than the previous ones to perform the fulcrum effect. They are
 97 unlimited to a specific kinematic structure since they impose the bilateral constraints in the task space
 98 (i.e., constraints on the interaction matrix as $\dot{\mathbf{s}} = \mathbf{L}_s \mathbf{v}_e$). Indeed, the interaction matrix $\mathbf{L}_s \in \mathbb{R}^{m \times 6}$
 99 relates the features velocities $\dot{\mathbf{s}} \in \mathbb{R}^{m \times 1}$ and the end-effector twist vector. Such formulation does not
 100 necessarily require an accurate knowledge of the robot inverse kinematics.

101 Moreover, the previous methods applied a trajectory tracking scheme as a secondary task.
 102 However, trajectory tracking methods are less appropriate for medical applications as discussed
 103 in ref. [23], since the trajectory controller is limited in terms of accuracy and stability (e.g., when
 104 dealing with complex geometric curves with high curvatures) and more complicated to implement
 105 compared to a path-following scheme. Thereby, the previous work⁶ assembled individual tasks
 106 (i.e., both the RCM and the path-following tasks) to perform a complex motion within the patient
 107 body by handling a straight tool. The projection gradient technique was also applied to guaran-
 108 tee the hierarchy/priority between the various tasks. Despite that this controller cannot manage the
 109 UCM case.

110 In the literature, constraining motion in a given direction was initially introduced by Rosenberg²⁴
 111 to formulate the so-called *virtual fixtures*. This method was used to guide a teleoperated robot by
 112 applying a hybrid force/motion control. Furthermore, the various techniques associated with the
 113 virtual fixtures in medical applications are presented in a very interesting survey.²⁵ Note that the
 114 admittance control is derived from the virtual fixture method. It is also based on the kinematic
 115 and dynamic models of the robot as well as the interaction model with its environment. Indeed,
 116 this technique regulates the velocities/forces interacted with the environment by imposing a devi-
 117 ation from the desired motion. Besides that, it is considered as an indirect force control (i.e., the
 118 force measurement is not performed). Finally, this approach was implemented in the described work
 119 in this paper by deducing the interaction matrix that calculates the control velocities for achieving
 120 the UCM.

121 2.2. Contributions

122 This paper has the objective to formulate the UCM movement in an easy and versatile geomet-
 123 ric form. Indeed, the previous work in ref. [6] handles a straight tool to perform a path following
 124 under bilateral constraint, while this article extended the controller capability by guiding a curved

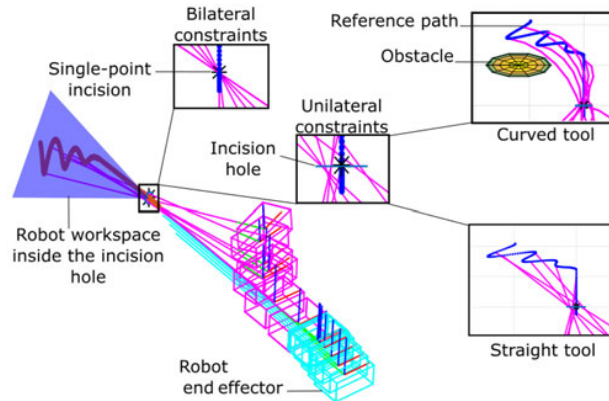


Fig. 3. A synthetic view of the various cases that can be handled by the proposed controller.

125 instrument to achieve a path following under unilateral constraint. The mathematical formulation in
 126 the next sections shows that a straight tool can be considered as an especial case of a curved one.
 127 Consequently, the new controller becomes more generic. It deduces the spatial velocity of the robot
 128 end effector for manipulating a rigid instrument through an orifice whose diameter can either be
 129 equal or larger than that of the tool.

130 Note that the curved geometry provides the system/surgeon with more dexterity for avoiding
 131 obstacles as shown in Fig. 3. This figure presents a general case where the tool first moves from its
 132 initial position toward the entrance of the incision hole (i.e., *outside phase*). Then, in a second phase
 133 (i.e., the *inside phase*), the tool follows a 3D path (e.g., an incision task, represented here without loss
 134 of generality by a spiral) under the constraints imposed by the incision hole. The workspace inside
 135 the incision hole is represented by the blue triangle in Fig. 3. Zoom was made on the incision hole
 136 in order to demonstrate the difference between the RCM and UCM movements. The upper left zoom
 137 plot entitled “*Bilateral constraints*” in this figure shows how the tool body always passes through the
 138 orifice center point. On the opposite, the central zoom plot entitled “*Unilateral Constraints*” demon-
 139 strates that the tool body moves within the orifice whose wall is represented by a blue horizontal
 140 line in this plot. The right zoom plots reveal how a curved tool has a better dexterity for avoiding
 141 obstacles, compared to a straight tool, under the unilateral constraints.

142 3. Background: Time-Independent Control of Straight Tools along a Surgical Path under 143 Bilateral Constraints

144 3.1. Notations

145 In this paper, we opted for the notations and symbols summarized in Table I. For instance, bold
 146 nonitalic letters denote vectors (e.g., \mathbf{x}) and bold nonitalic uppercase letters represent matrices (e.g.,
 147 \mathbf{X}). Scalar values and continuous-time functions will be denoted by italic letters (e.g., x). Also, a
 148 vector distance from a point a to a point b is written as a vector by \mathcal{V}_{ab} . The frame attached to an
 149 origin \mathcal{O}_i is represented by \mathfrak{R}_i .

150 3.2. Medical gesture as a 3D path-following scheme

151 In MIS applications, the physician may need to excise or scan a pathological tissue by using an abla-
 152 tion tool (e.g., laser) or an optical endoscopic probe, respectively. Indeed, for better surgical task
 153 achievement, the tool tip should move accurately on the tissue with a velocity that is mostly indepen-
 154 dent of the path geometrical shape. Furthermore, the clinician does not possess precise knowledge of
 155 the tool tip velocity. Furthermore, he/she may need to change this velocity online (while the robot is
 156 executing the reference geometrical curve).

157 Consequently, instead of using a 3D trajectory tracking technique, we opted for a 3D path-
 158 following scheme more adequate to the clinical requirements.²³ Recently, in ref. [26], we demon-
 159 strated the preliminary benefits of this approach in the case of middle ear surgery (using a laboratory

Table I. Notations summary.

Symbol	Description
\mathcal{O}_i	Origin point of a 3D frame;
\mathfrak{R}_i	Frame attached to the origin point \mathcal{O}_i ;
${}^i\mathbf{y}$	y-axis (basis vector) of \mathfrak{R}_i ;
$\mathbf{I}_{n \times m}$	$n \times m$ identity matrix;
$\mathbf{X}_{n \times m}$	$n \times m$ matrix;
$\mathbf{x}, \mathbf{x}^\top$	Vector and its transpose, respectively;
$\mathbf{x}_1 \times \mathbf{x}_2$	Cross product between vectors \mathbf{x}_1 and \mathbf{x}_2 ;
$[\mathbf{x}]_\times$	Skew matrix associated to the vector \mathbf{x} ;
$\ \mathbf{x}\ $	Euclidean norm of the vector \mathbf{x} ;
$\dot{\mathbf{x}}$	Time derivation of the vector \mathbf{x} ;
\mathcal{V}_{ab}	Vector between the \mathcal{O}_a and \mathcal{O}_b ;
$\dot{\mathcal{V}}_{ab}$	Time derivation of the vector \mathcal{V}_{ab} ;
${}^i\mathbf{u}_{ab}$	Unit vector of ${}^i\mathbf{ab}$ expressed in \mathfrak{R}_i ;
${}^i\dot{\mathbf{u}}_{ab}$	Time derivative of the unit vector ${}^i\mathbf{u}_{ab}$;
s_t	Length of a curve arc;
\dot{s}_t	Curvilinear speed of a point \mathbf{p} ;
$S_t(s_t)$	Tool curved shape function of s_t ;
\mathbf{p}_t'	Point along a curve (curved tool);
${}^e\mathbf{k}_t$	Instantaneous tangential unit vector of the tool shape;
\mathbf{r}_{C_t}	Curve (curved tool) radius at a given point;
\mathbf{C}_t	Curvature of the tool which is the inverse of the radius \mathbf{r}_{C_t} ;
$\{\mathbf{k}, \mathbf{j}, \mathbf{i}\}$	Constructed basis using three unit vectors;
\mathbf{d}_{rcm}	Linear error of alignment task;
d_{rcm}	Projection of \mathbf{d}_{rcm} along an axis;
d_{min}, d_{max}	Minimum and maximum distance d_{rcm} in case of UCM method, respectively;
\mathbf{d}_{pf}	Path-following error;
\mathbf{p}_p	Projected 2D point onto the path S_p to be followed;
Δt	Small time step;
\mathbf{e}_{rcm}	Angular error of the alignment task;
$\dot{\mathbf{e}}_{rcm}$	Time derivative of the angular RCM error;
${}^i\mathbf{v}_j$	Linear velocity of j expressed in i ;
${}^i\omega_j$	Angular velocity of j expressed in i ;
${}^i\mathbf{v}_i$	Twist velocity vector of i composed of (${}^i\mathbf{v}_i = [{}^i\mathbf{v}_i; {}^i\omega_i] \in \mathbb{R}^{6 \times 1}$);
\mathbf{v}_{adv}	Advance velocity along a path;
\mathbf{v}_{ret}	Regulation velocity of the tool deviation;
$\mathbf{L}_{e_{rcm}}$	3×6 interaction matrix of the alignment task;
$\mathbf{L}_{e_{rcm}}^\dagger$	6×3 inverse matrix of $\mathbf{L}_{e_{rcm}}$;
λ	A positive scalar gain for the alignment task;
α_{obs}	Stiffness of a virtual spring;
$\sigma_{min}, \sigma_{max}$	Minimum and maximum stiffness of the virtual spring, respectively;
σ_{step}	Step of change of the virtual spring stiffness;
α, β	Gain coefficients for adjusting the priority between \mathbf{v}_{adv} and \mathbf{v}_{ret} .

160 test bench). Thus, this section recalls the formulation of the 3D path-following controller which is
 161 based on the *Frenet–Serret* frame representation.

162 Let us consider that the path-following error \mathbf{d}_{pf} as depicted in Fig. 4(a). This error is determined
 163 by projecting the tool tip \mathcal{O}_t onto the reference path $S_p(s_p)$, which results in a projected point \mathbf{p}_p .
 164 Thus, \mathbf{d}_{pf} is obtained by

$$\mathbf{d}_{pf} = \mathcal{O}_t - \mathbf{p}_p. \quad (1)$$

165 At present, the challenge is to find the adequate controller that deduces the tool tip linear velocity
 166 \mathbf{v}_t for minimizing the projection distance \mathbf{d}_{pf} expressed in (1). To tackle this, the proposed controller
 167 decomposes the latter velocity \mathbf{v}_t into two components (Fig. 4(b)): (i) the advance velocity \mathbf{v}_{adv} along
 the path and (ii) the return velocity \mathbf{v}_{ret} for regulating the tool deviation from the path.

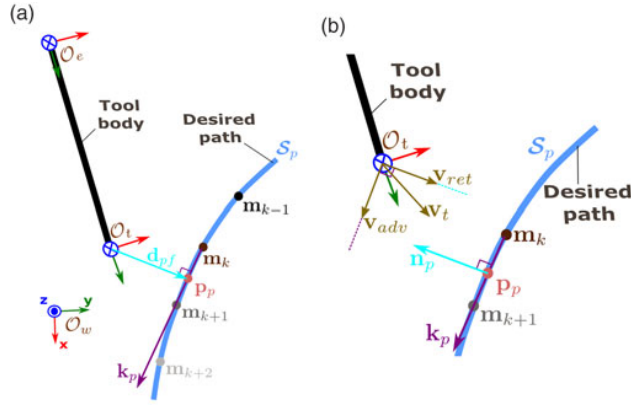


Fig. 4. The different reference frames and notions used during the path-following controller design, where (a) projection of the tool tip onto a geometric curve and (b) concept of path-following approach.

168 One can formulate the previous concept as follows:

$$\mathbf{v}_t = \underbrace{\alpha \mathbf{k}_p}_{=\mathbf{v}_{adv}} + \underbrace{\beta \mathbf{d}_{pf}}_{=\mathbf{v}_{ret}} \quad (2)$$

169 whereby α and β are the gain coefficients for adjusting the priority between the advance and return
 170 velocities, respectively, and \mathbf{k}_p is the instantaneous tangential unit vector to the geometric curve
 171 (Fig. 4(b)).

172 A possible option is imposing a constant velocity to the tool as $\|\mathbf{v}_t\|^2 = v_{tis}^2$ in order to deduce the
 173 values of the gain coefficients α and β . Indeed, the velocity v_{tis} depends on the interaction between
 174 the surgical tool and the tissue homogeneity. Therefore, (2) can be reformulated as follows:

$$v_{tis}^2 = \alpha^2 \underbrace{\|\mathbf{k}_p\|^2}_{=1} + \beta^2 \underbrace{\|\mathbf{d}_{pf}\|^2}_{=\|\mathbf{v}_{ret}\|^2}. \quad (3)$$

175 So,

$$\text{if } \begin{cases} \|\mathbf{v}_{ret}\|^2 < v_{tis}^2, \\ \|\mathbf{v}_{ret}\|^2 > v_{tis}^2, \end{cases} \begin{cases} \beta = \text{constant} \\ \alpha = \sqrt{\|\mathbf{v}_{ret}\|^2 + v_{tis}^2} \\ \beta = \text{constant} \\ \alpha = 0 \end{cases}. \quad (4)$$

176 The choice of the gain parameters is determined in function of the clinical needs (e.g., the velocity
 177 of the surgical tool with respect to the tissue type). For instance, if the tool is not far from the
 178 desired path, the first condition in (4) is chosen. Otherwise, the priority is returning the tool tip to the
 179 reference path (i.e., second condition in (4)).

180 The resultant control velocity of the tool tip (2) could be represented with respect to any desired
 181 frame. Then, by choosing the end-effector frame \mathcal{R}_e , the twist velocity of end effector ${}^e\mathbf{v}_e \in \mathbb{R}^{6 \times 1}$ is
 182 related to the tool tip linear velocity ${}^e\mathbf{v}_t \in \mathbb{R}^{3 \times 1}$ by the interaction matrix $\mathbf{L}_{e_{pf}} \in \mathbb{R}^{3 \times 6}$ as follows:

$${}^e\mathbf{v}_t = \underbrace{\left(\mathbf{I}_{3 \times 3} \quad -[{}^e\mathcal{V}_{et}]_{\times} \right)}_{\mathbf{L}_{e_{pf}}} \underbrace{\begin{pmatrix} {}^e\mathbf{v}_e \\ {}^e\boldsymbol{\omega}_e \end{pmatrix}}_{{}^e\mathbf{v}_e} \quad (5)$$

183 whereby $[{}^e\mathcal{V}_{et}]_{\times}$ is the antisymmetric matrix of the vector ${}^e\mathcal{V}_{et}$ which begins at the end effector \mathcal{O}_e
 184 and ends at the tool tip \mathcal{O}_t .

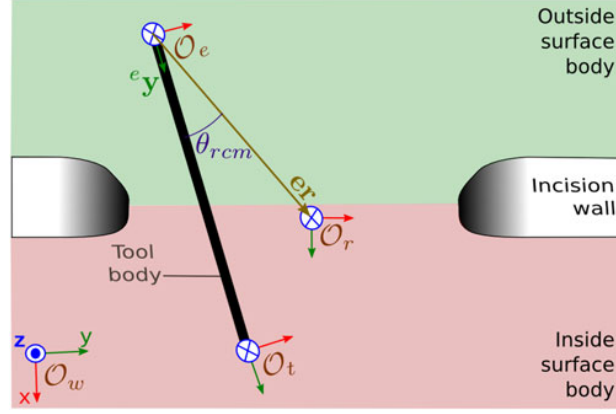


Fig. 5. The different reference frames and notions used within the formulation of the RCM (bilateral) problem.

185 3.3. RCM with straight tool

186 First, let us consider the following reference frames that are necessary to express the different
187 transformations:

- 188 • \mathfrak{R}_e attached to the robot end effector, having as origin the point \mathcal{O}_e ;
- 189 • \mathfrak{R}_t linked to the surgical tool with \mathcal{O}_t , the related origin point of the frame;
- 190 • \mathfrak{R}_r fixed at the center of the incision point or natural orifice denoted \mathcal{O}_r .

191

192 In ref. [6], the alignment condition of RCM task was proposed as the geodesic error between two
193 vectors: (i) the unit vector of ${}^e\mathcal{V}_{er}$ (i.e., ${}^e\mathbf{u}_{er}$) which is formed between the origin points \mathcal{O}_e
194 and \mathcal{O}_r (see Fig. 5) and (ii) the y-component of the end-effector frame ${}^e\mathbf{y}$. These vectors are expressed
195 with respect to the end-effector frame \mathfrak{R}_e (i.e., the left superscript). The RCM angular error is thus
196 formulated as the cross product given by

$$\mathbf{e}_{rcm} = {}^e\mathbf{y} \times {}^e\mathbf{u}_{er}. \quad (6)$$

197 Recall that a velocity controller is needed to reduce the RCM angular error. Thereby, the time
198 derivative of the unit vector ${}^e\mathbf{u}_{er}$ is computed as

$${}^e\dot{\mathbf{u}}_{er} = \left(\frac{\mathbf{I}_{3 \times 3}}{\|{}^e\mathcal{V}_{er}\|} - \frac{{}^e\mathbf{u}_{er} {}^e\mathbf{u}_{er}^\top}{\|{}^e\mathcal{V}_{er}\|} \right) {}^e\dot{\mathcal{V}}_{er} \quad (7)$$

199 where $\|\mathbf{x}\|$, \mathbf{x}^\top , and $[\mathbf{x}]_\times$ are the Euclidean norm, transpose, and the antisymmetric matrix associated
200 with the vector \mathbf{n} , respectively, and \mathbf{I} is a 3×3 identity matrix.

201 Besides that, the term ${}^e\dot{\mathcal{V}}_{er}$ in the latter equation represents the linear velocity of the incision frame
202 \mathfrak{R}_r with respect to the end-effector frame \mathfrak{R}_e (i.e., ${}^e\dot{\mathcal{V}}_{er} = {}^e\mathbf{v}_r$). This linear velocity ${}^e\mathbf{v}_r$ can be related
203 to the end-effector twist vector ${}^e\mathbf{v}_e$ as

$${}^e\mathbf{v}_r = \left(\mathbf{I}_{3 \times 3} \quad -[{}^e\mathcal{V}_{er}]_\times \right) \underbrace{\begin{pmatrix} {}^e\mathbf{v}_e \\ {}^e\omega_e \end{pmatrix}}_{{}^e\mathbf{v}_e}. \quad (8)$$

204 Consequently, the unit vector ${}^e\dot{\mathbf{u}}_{er}$ is reformulated as

$${}^e\dot{\mathbf{u}}_{er} = \underbrace{\frac{-1}{\|{}^e\mathcal{V}_{er}\|} \left(\mathbf{I}_{3 \times 3} - {}^e\mathbf{u}_{er} {}^e\mathbf{u}_{er}^\top \right) \left(\mathbf{I}_{3 \times 3} \quad -[{}^e\mathcal{V}_{er}]_\times \right)}_{\mathbf{L}_{uer}} {}^e\mathbf{v}_e \quad (9)$$

205 where $\mathbf{L}_{uer} \in \mathbb{R}^{3 \times 6}$ is the interaction matrix that relates the rate of change of the unit vector ${}^e\dot{\mathbf{u}}_{er}$ to the
206 spatial velocity of the end effector expressed in its own frame ${}^e\mathbf{v}_e$.

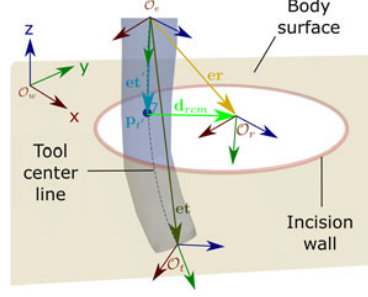


Fig. 6. A conceptual scheme to show the notions used for a curved tool with respect to the incision hole.

207 Note that a negative sign was added to (9) because the incision point frame \mathfrak{R}_r moves in the
208 opposite direction of that of the end effector \mathfrak{R}_e for reducing the RCM error.

209 4. Time-Independent Control of a Curved Tool along a Surgical Path under Bilateral 210 Constraints

211 The alignment condition of the tool body with the incision point in (6) is only valid in case of a
212 straight tool since the vector ${}^e\mathcal{V}_{et}$ is always aligned with the basis ${}^e\mathbf{y}$. Thereby, if the tool is curved,
213 the vector ${}^e\mathcal{V}_{et}$ is no longer aligned with the basis ${}^e\mathbf{y}$ (Fig. 6).

214 As a result, the alignment condition in (6) can be modified with the aim to be more generic for
215 any tool shape. One can tackle this, by tracking \mathbf{p}_t which is the orthogonal projection of the incision
216 point \mathcal{O}_r onto the curved tool body. The resultant projection distance \mathbf{d}_{rcm} can be considered as the
217 RCM lateral error. It is thus evaluated as follows:

$$\mathbf{d}_{rcm} = \left(\mathbf{I}_{3 \times 3} - {}^e\mathbf{u}_{et'} {}^e\mathbf{u}_{et'}^\top \right) {}^e\mathcal{V}_{er} \quad (10)$$

218 whereby ${}^e\mathbf{u}_{et'}$ is the unit vector of ${}^e\mathcal{V}_{et'}$, which is formed between the origin point \mathcal{O}_e and the projected
219 point \mathbf{p}_t .

220 After deducing the projected point \mathbf{p}_t , the unit vector ${}^e\mathbf{u}_{et'}$ replaces the vector ${}^e\mathbf{y}$ in (6).
221 Consequently, the RCM angular error can be rewritten as

$$\mathbf{e}_{rcm} = {}^e\mathbf{u}_{et'} \times {}^e\mathbf{u}_{er}, \quad (11)$$

222 and its time derivative is computed as

$$\dot{\mathbf{e}}_{rcm} = {}^e\mathbf{u}_{et'} \times {}^e\dot{\mathbf{u}}_{er} + \dot{{}^e\mathbf{u}}_{et'} \times {}^e\mathbf{u}_{er}. \quad (12)$$

223 *Proposition 1.* The rate of change of the alignment task is obtained as follows:

$$\dot{\mathbf{e}}_{rcm} = \underbrace{\left([{}^e\mathbf{u}_{et'}]_\times \mathbf{L}_{u_{er}} - [{}^e\mathbf{u}_{er}]_\times \mathbf{L}_{u_{et'}} \right)}_{\mathbf{L}_{e_{rcm}}} {}^e\mathbf{v}_e \quad (13)$$

224 where $\mathbf{L}_{e_{rcm}} \in \mathbb{R}^{3 \times 6}$ is the interaction matrix of the alignment task that relates the rate of change of
225 the RCM angular error $\dot{\mathbf{e}}_{rcm}$ with the end-effector twist vector ${}^e\mathbf{v}_e$.

226 *Proof.* In order to demonstrate Proposition 1, it is required to know all components of equation
227 (12). The unit vector ${}^e\mathbf{u}_{er}$ can be determined trivially while its time derivative $\dot{{}^e\mathbf{u}}_{er}$ is formulated in
228 (9). The vector $\dot{{}^e\mathbf{u}}_{et'} = \mathbf{L}_{u_{et'}} {}^e\mathbf{v}_e$ is formally deduced in a similar way to (9). By substituting these
229 variables in (12), we can find (13). \square

230 Now, the expression of $\mathbf{L}_{u_{et'}}$ needs to be expressed.

231 **Lemma 1.** The interaction matrix $\mathbf{L}_{u_{et'}}$ is computed as

$$\mathbf{L}_{u_{et'}} = \frac{1}{\|{}^e\mathbf{et}'\|} \left(\mathbf{I}_{3 \times 3} - {}^e\mathbf{u}_{et'} {}^e\mathbf{u}_{et'}^\top \right) \mathbf{L}_{et'} \quad (14)$$

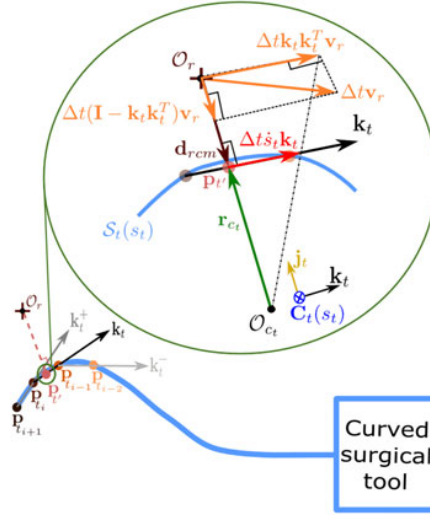


Fig. 7. The geometrical description for (i) projection of the incision center point \mathcal{O}_r along the curved tool and (ii) computation of the velocity of the projected point \mathbf{p}_r along the curved tool.

232 where $\mathbf{L}_{et'}$ is a 3×6 interaction matrix that relates the rate of change ${}^e\dot{\mathcal{V}}_{et'}$ with the end-effector twist
 233 vector ${}^e\mathbf{v}_e$.

234 *Proof.* The time derivative of the unit vector ${}^e\mathbf{u}_{et'}$ is deduced similar to (7) as

$${}^e\dot{\mathbf{u}}_{et'} = \frac{1}{\|{}^e\mathbf{u}_{et'}\|} \left(\mathbf{I}_{3 \times 3} - {}^e\mathbf{u}_{et'} {}^e\mathbf{u}_{et'}^T \right) {}^e\dot{\mathcal{V}}_{et'}. \quad (15)$$

235 The time derivative of the vector ${}^e\mathcal{V}_{et'}$ represents the velocity of the projection point ${}^e\mathbf{p}_r$ along the
 236 tool shape $S_t(s_t)$, which is a function of the curve arc length s_t . It is also related to the end-effector
 237 twist vector ${}^e\mathbf{v}_e$ as follows:

$${}^e\dot{\mathcal{V}}_{et'} = \mathbf{L}_{et'} {}^e\mathbf{v}_e. \quad (16)$$

238 By substituting the latter equation in (15), the matrix $\mathbf{L}_{u_{et'}}$ is deduced as (14). \square

239 The next lemma shows how to calculate the interaction matrix $\mathbf{L}_{et'}$.

240 **Lemma 2.** The interaction matrix $\mathbf{L}_{et'}$ is computed as follows:

$$\mathbf{L}_{et'} = \frac{{}^e\mathbf{k}_t {}^e\mathbf{k}_t^T}{1 + \mathbf{d}_{rcm}^T (\mathbf{C}_t(s_t) \times {}^e\mathbf{k}_t)} \left(\mathbf{I}_{3 \times 3} - [{}^e\mathcal{V}_{er}]_{\times} \right) \quad (17)$$

241 whereby \mathbf{C}_t is the tool curvature, and ${}^e\mathbf{k}_t$ is the instantaneous tangential unit vector on the tool shape.

242 *Proof.* The time derivative of the vector ${}^e\mathcal{V}_{et'}$ can be determined as

$$\begin{aligned} 243 \quad {}^e\dot{\mathcal{V}}_{et'} &= \frac{\partial {}^e\mathcal{V}_{et'}}{\partial s_t} \frac{ds_t}{dt} \\ 244 \quad &= {}^e\mathbf{k}_t \dot{s}_t \end{aligned} \quad (18)$$

245 The time derivative of s_t is nothing more than the curvilinear speed of \mathbf{p}_r along the curved tool.
 246 Indeed, the tool shape is defined by the tool curvature \mathbf{C}_t , which is determined by a radius of curvature
 247 \mathbf{r}_{C_t} and its center point \mathcal{O}_{C_t} , as depicted in Fig. 7, while the unit vector ${}^e\mathbf{k}_t$ could be approximated by
 248 two consecutive sample points on the tool body.

249 Now, the main problem becomes how to deduce the speed \dot{s}_t in order to determine the time deriva-
 250 tive ${}^e\dot{\mathcal{V}}_{et'}$. Therefore, a reference frame is placed at the center point \mathcal{O}_{C_t} , and its basis is formed by
 $\{{}^e\mathbf{k}_t, {}^e\mathbf{j}_t, {}^e\mathbf{i}_t\}$ as

$${}^e \mathbf{k}_t = \frac{{}^e \mathbf{p}_{t-1} - {}^e \mathbf{p}_t}{\|{}^e \mathbf{p}_{t-1} - {}^e \mathbf{p}_t\|}, \quad (19)$$

$${}^e \mathbf{j}_t = \frac{\mathbf{r}_{C_t}}{\|\mathbf{r}_{C_t}\|}, \quad (20)$$

$${}^e \mathbf{i}_t = {}^e \mathbf{j}_t \times {}^e \mathbf{k}_t. \quad (21)$$

254 The radius of curvature \mathbf{r}_{C_t} is in the same direction as the basis ${}^e \mathbf{j}_t$ (Fig. 7), then it is defined as

$$\mathbf{r}_{C_t} = r_{C_t} {}^e \mathbf{j}_t, \quad (22)$$

255 with $r_{C_t} = \|\mathbf{r}_{C_t}\| \in \mathbb{R}^+$.

256 Furthermore, the vector \mathbf{d}_{rcm} is also collinear with ${}^e \mathbf{j}_t$, and its direction could be either in the
257 same or in the opposite direction with/to that of the basis ${}^e \mathbf{j}_t$. Consequently, the vector \mathbf{d}_{rcm} could be
258 reformulated as follows:

$$\mathbf{d}_{rcm} = \underbrace{\mathbf{d}_{rcm}^\top}_{=d_{rcm}} {}^e \mathbf{j}_t, \quad (23)$$

259 with

$$d_{rcm} = \frac{\mathbf{d}_{rcm}^\top \mathbf{r}_{C_t}}{\|\mathbf{r}_{C_t}\|} \in \mathbb{R}. \quad (24)$$

260 Furthermore, the curvature \mathbf{C}_t is defined in the same direction as ${}^e \mathbf{i}_t$, since

$$\mathbf{C}_t(s_t) \times \mathbf{r}_{C_t} = {}^e \mathbf{k}_t, \quad (25)$$

261 and

$$\begin{aligned} \|\mathbf{C}_t(s_t)\| &= \frac{1}{\|\mathbf{r}_{C_t}\|} \\ &= C_t \in \mathbb{R}^+, \end{aligned} \quad (26)$$

264 thereby,

$$\mathbf{C}_t(s_t) = C_t {}^e \mathbf{i}_t. \quad (27)$$

265 As a result, the instantaneous curvature is calculated analytically by substituting (21) in the latter
266 equation as

$$\mathbf{C}_t(s_t) = \frac{\mathbf{r}_{C_t} \times {}^e \mathbf{k}_t}{\|\mathbf{r}_{C_t}\|^2}. \quad (28)$$

267 Let us assume a finite displacement applied to the incision center point \mathcal{O}_r at a velocity ${}^e \mathbf{v}_r$ during
268 a small period Δt , as depicted in Fig. 7. The resultant displacement from the linear velocity (${}^e \mathbf{v}_r \Delta t$)
269 of the incision frame is decomposed into:

270 1. A first component

$${}^e \mathbf{v}_{rk} = {}^e \mathbf{k}_t {}^e \mathbf{k}_t^\top {}^e \mathbf{v}_r \Delta t \quad (29)$$

271 which represents the projected component of ${}^e \mathbf{v}_r$ onto the vector ${}^e \mathbf{k}_t$ and it effects on the progress
272 of \mathbf{p}_r along the tool shape, and

273 2. A second component

$${}^e \mathbf{v}_{rj} = (\mathbf{I} - {}^e \mathbf{k}_t {}^e \mathbf{k}_t^\top) {}^e \mathbf{v}_r \Delta t \quad (30)$$

274 which is the complement of the first component and it acts directly on the distance \mathbf{d}_{rcm} .

275 The first component is used to express analytically the curvilinear speed \dot{s}_t based on *Thales* the-
276 orem. The position of the projected point $\mathbf{p}_r(t + \Delta t)$ is found by the intersection of the radial line
passing through the vector $(\mathcal{O}_{c_t}, \mathcal{O}_r + \Delta t {}^e \mathbf{k}_t {}^e \mathbf{k}_t^\top {}^e \mathbf{v}_r)$, as shown in Fig. 8. Therefore, the two triangles

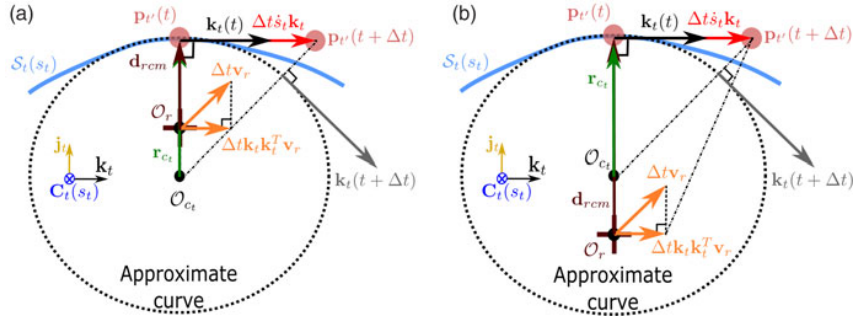


Fig. 9. Zoom on the geometric description of the tool curvature as well as the incision point \mathcal{O}_r at the instantaneous positions where (a) the point \mathcal{O}_r is located between the two points \mathbf{p}_r and \mathcal{O}_c and (b) the point \mathcal{O}_c is located within the segment formed between \mathcal{O}_r and \mathbf{p}_r .

287 Considering that ${}^e \mathbf{j}_t^\top {}^e \mathbf{j}_t = 1$, then (36) becomes

$$d_{rcm} \mathbf{C}_t = -\mathbf{d}_{rcm}^\top \left(\mathbf{C}_t(s_t) \times {}^e \mathbf{k}_t \right). \quad (37)$$

288 Furthermore, by substituting (37) in (34) allows deducing the speed \dot{s}_t as

$$\dot{s}_t = \frac{{}^e \mathbf{k}_t^\top {}^e \mathbf{v}_r}{1 + \mathbf{d}_{rcm}^\top \left(\mathbf{C}_t(s_t) \times {}^e \mathbf{k}_t \right)}. \quad (38)$$

289 After the formulation of the curvilinear speed \dot{s}_t , the velocity of projected point ${}^e \dot{\mathcal{V}}_{et'}$ is determined
290 by injecting (38) in (18) as

$${}^e \dot{\mathcal{V}}_{et'} = \frac{{}^e \mathbf{k}_t {}^e \mathbf{k}_t^\top}{1 + \mathbf{d}_{rcm}^\top \left(\mathbf{C}_t(s_t) \times {}^e \mathbf{k}_t \right)} {}^e \mathbf{v}_r. \quad (39)$$

291 Finally, the matrix $\mathbf{L}_{et'}$ is expressed by replacing (8) in the latter equation. \square

292 The latter solution is valid if and only if the projected distance \mathbf{d}_{rcm} is smaller than the radius
293 ${}^e \mathbf{r}_{C_t}$ (Fig. 8) because the *Thales* theorem cannot be used directly to formulate similar triangles. As
294 consequence, it is necessary to satisfy the following conditions (see, Fig. 8)

295 $\star \mathbf{p}_r \in [\mathcal{O}_r, \mathcal{O}_c]$, and $\mathbf{d}_{rcm} \in \mathbb{R}^-$

296 or (as depicted in Fig. 9a)

297 $\star \mathcal{O}_r \in [\mathbf{p}_r, \mathcal{O}_c]$, and $\mathbf{d}_{rcm} \in \mathbb{R}^+$

298 One can notice that when $\mathbf{d}_{rcm} = \mathbf{r}_{C_t}$, there is a numerical singularity because the right-hand side of
299 (32) is divided by zero. Thereby, the implementation of RCM controller should consider this singular
300 case.

301 Figure 9b shows another special case which could happen when

302 $\star \mathcal{O}_c \in [\mathcal{O}_r, \mathbf{p}_r]$ and $\mathbf{d}_{rcm} > \mathbf{r}_{C_t}$.

303 However, this kind of situation has not a simple geometric construction to find out an analytical
304 expression of the curvilinear velocity \dot{s}_t because the modeling of similar triangles cannot be identified
305 in the aim to apply the *Thales* theorem. Indeed, this case uses a highly curved tool, which is not
306 treated in this work, because it requires a specific numerical solution and also because these types of
307 instruments are uncommon in surgery. For instance, if the vector distance \mathbf{d}_{rcm} is around 1 mm, to
308 satisfy this special case, the curvature radius \mathbf{r}_{C_t} should be less than 1 mm.

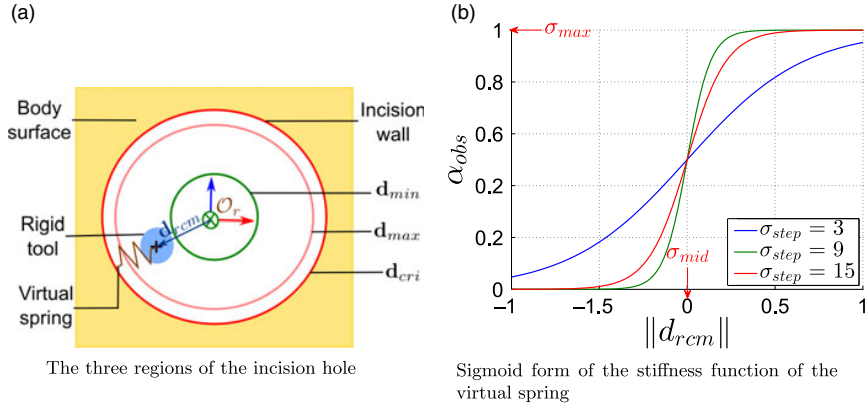


Fig. 10. A conceptual scheme of UCM movement.

309 *Control of the error:* A conventional proportional controller is applied to reduce exponentially the
 310 alignment task error as

$$\begin{aligned} 311 \quad \dot{\mathbf{e}}_{rcm} &= \mathbf{L}_{e_{rcm}} \mathbf{e}_{\underline{v}_e} \\ 312 \quad &= -\lambda \mathbf{e}_{rcm}. \end{aligned} \quad (40)$$

313 Thereby, the twist velocity of the end effector is determined as follows:

$$314 \quad \mathbf{e}_{\underline{v}_e} = -\lambda \mathbf{L}_{e_{rcm}}^\dagger \mathbf{e}_{rcm} \quad (41)$$

314 where $\mathbf{L}_{e_{rcm}}^\dagger$ is the inverse matrix of $\mathbf{L}_{e_{rcm}}$ and λ is a positive scalar gain to tune the decreasing rate of
 315 the angular error between both vectors ${}^e \mathbf{u}_{ef}$ and ${}^e \mathbf{u}_{er}$. Equation (40) is not only valid for a curved
 316 tool, but it is also applicable for a straight tool that can be considered as a special case.

317 5. Time-Independent Control of a Curved Tool along a Surgical Path under Unilateral 318 Constraints

319 5.1. Unilaterally constrained motion

320 An intuitive solution is proposed to formulate the UCM issue by inserting a virtual spring between
 321 the tool body and the incision wall. Thereby, the incision diameter is divided into three regions as
 322 depicted in Fig. 10(a):

- 323 ★ a *free region* around the point \mathcal{O}_r by a minimum distance d_{min} , where the virtual spring is
- 324 deactivated and the tool is free to move without any constraints;
- 325 ★ a *safe region* bounded between the minimum distance d_{min} and a maximum one d_{max} , where the
- 326 virtual spring is activated and its stiffness σ_{obs} increases gradually (with a step of σ_{step}) when the
- 327 tool body approaches to d_{max} ;
- 328 ★ a *critical region* where the stiffness of the virtual spring achieves its maximum value when the
- 329 tool body passes d_{max} .

330 *Control of the error:* Admittance control is added to the control law (40) by inserting a virtual spring
 331 characterized by a stiffness α_{obs} . It is hence formulated as

$$332 \quad \mathbf{L}_{e_{rcm}} \mathbf{e}_{\underline{v}_e} = -\alpha_{obs} \lambda \mathbf{e}_{rcm}. \quad (42)$$

332 This virtual spring behaves like a repulsive force to keep the tool body away from the incision wall.
 333 Its stiffness α_{obs} is chosen as a sigmoid function (Fig. 10(b)) for obtaining a continuous differentiable
 transition between the three distinct regions. Therefore, the stiffness α_{obs} is chosen as

$$\begin{cases} 0 & \|\mathbf{d}_{rcm}\| \leq d_{min} \\ \frac{\sigma_{max}}{1 + e^{\left(\frac{\sigma_{step}}{\|\mathbf{d}_{rcm}\| - \sigma_{min}}\right)}} & d_{min} < \|\mathbf{d}_{rcm}\| < d_{max} \\ 1 & d_{max} \leq \|\mathbf{d}_{rcm}\| \leq d_{cri} \end{cases}. \quad (43)$$

334 The latter behavior depends on the projected distance \mathbf{d}_{rcm} , which represents the tool body position
 335 with respect to the incision center point \mathcal{O}_r (Fig. 10(a)). Finally, the control twist vector of the end
 336 effector is calculated as

$${}^e \underline{\mathbf{v}}_e = -\alpha_{obs} \lambda \mathbf{L}_{e_{rcm}}^\dagger \mathbf{e}_{rcm}. \quad (44)$$

337 5.2. Hierarchical assembly of subtasks

338 The task priority controller arranges the different subtasks depending on the relative pose of the
 339 surgical tool with respect to the incision hole. The controller deduces the spatial velocity of the
 340 robot end effector. Indeed, the tool motion is mainly divided into two phases. The *outside phase* is
 341 the first stage where the tool moves from its initial pose toward the incision hole. During this first
 342 phase, it is required that (i) the controller reduces the alignment error between the tool body and
 343 the incision hole and (ii) the distance between the tool tip and the incision center point should be
 344 regulated toward zero.

345 The *inside phase* is the second stage where the tool tip begins to follow a reference path under
 346 the RCM/UCM constraints. During this second phase, the controller deduces the linear and angular
 347 velocities for regulating the alignment error and the path-following error.

348 The hierarchy between the different subtasks is modified to the criteria of each phase. Note that
 349 a hierarchy is achieved by applying the projection gradient technique,¹³ which allows projecting a
 350 secondary task in the null space of the first task. This projection provides an advantage to find out a
 351 solution that satisfies the secondary task without any conflict with the first one.

352 *Outside phase.* During this first phase, the alignment task (40) has the highest priority, while the
 353 second one is reducing the distance error $\mathbf{e}_{app} = {}^e \mathcal{V}_{tr}$ between the tool tip position \mathcal{O}_t and that of the
 354 trocar point \mathcal{O}_r . This error is regulated by a conventional proportional controller as

$$-\gamma \mathbf{e}_{app} = \underbrace{\left(\mathbf{I}_{3 \times 3} \quad - [{}^e \mathcal{V}_{er}]_{\times} \right)}_{\mathbf{L}_{e_{app}}} \underbrace{\begin{pmatrix} {}^e \mathbf{v}_e \\ {}^e \boldsymbol{\omega}_e \end{pmatrix}}_{{}^e \underline{\mathbf{v}}_e} \quad (45)$$

355 whereby γ is a positive gain factor that tunes the approach velocity to the trocar point, and $\mathbf{L}_{e_{app}} \in$
 356 $\mathbb{R}^{3 \times 6}$ is the interaction matrix of the approach task.

357 The control twist velocity of the end effector, which satisfies both tasks, is expressed as follows

$${}^e \underline{\mathbf{v}}_e = -\lambda \mathbf{L}_{e_{rcm}}^\dagger \mathbf{e}_{rcm} - \gamma \left(\mathbf{I}_{3 \times 3} - \mathbf{L}_{e_{rcm}}^\dagger \mathbf{L}_{e_{rcm}} \right) \mathbf{L}_{e_{app}}^\dagger \mathbf{e}_{app}. \quad (46)$$

358 *Inside phase with RCM movement:* Secondly, during this phase, the alignment task (40) is defined
 359 as the highest priority, while the path-following task (5) has a lower priority. Thus, the control twist
 360 velocity of the end effector is given by

$${}^e \underline{\mathbf{v}}_e = -\lambda \mathbf{L}_{e_{rcm}}^\dagger \mathbf{e}_{rcm} + \left(\mathbf{I}_{3 \times 3} - \mathbf{L}_{e_{rcm}}^\dagger \mathbf{L}_{e_{rcm}} \right) \mathbf{L}_{e_{pf}}^\dagger {}^e \mathbf{v}_t. \quad (47)$$

361 *Inside phase with UCM movement:* During this phase, the hierarchy is defined in terms of the tool
 362 position within the incision hole. Therefore, the incision hole is divided into two main regions:

363 ***** *Tool within the safe region:* When the norm of the projection distance $\|\mathbf{d}_{rcm}\|$ is smaller than the
 364 critical distance d_{cri} , the tool is free to move within this region. In this case, the first task is defined
 365 as the path following (5) and the lower priority is UCM task (42). Consequently, the end-effector
 366 twist vector is calculated as

$${}^e \underline{\mathbf{v}}_e = \mathbf{L}_{e_{pf}}^\dagger {}^e \mathbf{v}_t - \alpha_{obs} \lambda \left(\mathbf{I}_{3 \times 3} - \mathbf{L}_{e_{pf}}^\dagger \mathbf{L}_{e_{pf}} \right) \mathbf{L}_{e_{rcm}}^\dagger \mathbf{e}_{rcm}. \quad (48)$$

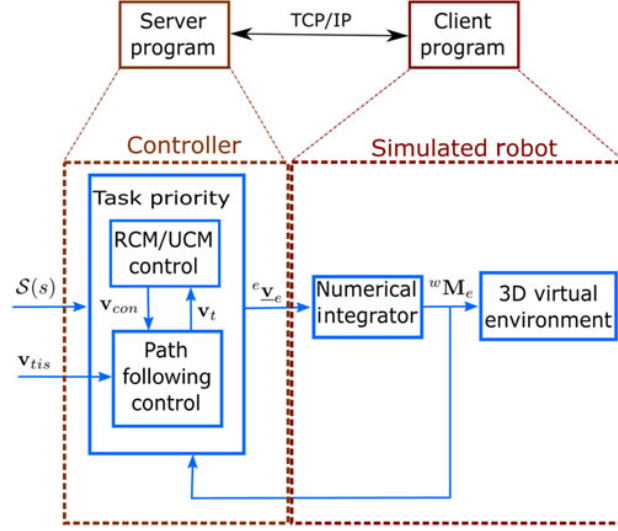


Fig. 11. Block diagram of the socket communication between the proposed controller and the simulated robot.

- 367 ★ *Tool within the dangerous region:* During this situation, the norm of the projection distance $\|\mathbf{d}_{rcm}\|$
 368 is bigger than the critical distance d_{cri} . As consequence, the UCM task becomes the first priority
 369 and the path following is considered as the second one. In fact, this solution brings back the tool
 370 into the safe region, and the end-effector twist vector is redefined as

$${}^e \mathbf{v}_e = -\alpha_{obs} \lambda \mathbf{L}_{e_{rcm}}^\dagger \mathbf{e}_{rcm} + \left(\mathbf{I}_{3 \times 3} - \mathbf{L}_{e_{rcm}}^\dagger \mathbf{L}_{e_{rcm}} \right) \mathbf{L}_{e_{pf}}^\dagger {}^e \mathbf{v}_t. \quad (49)$$

- 371 ★ If the tool passes the dangerous region for some reason, the controller switches to RCM movement
 372 (47) in order to bring back the tool as quickly as possible toward the safe region.

373 6. Numerical Validation

374 A numerical simulator was developed as the first step to validate the functioning of the different meth-
 375 ods before physical implementation. Therefore, the control architect was implemented to conceive
 376 the controller independent from the physical system (robot). Socket communication is implemented
 377 to establish the communication between the controller and the virtual robot, as depicted in Fig. 11.
 378 The next section will replace the simulated robot with a real robot.

379 The objective of the simulated tests discussed below is to demonstrate the influence of the model
 380 parameters (i.e., λ for the alignment task (40), γ for the approach task (45), and v_{tis} and β for the
 381 path-following controller (3)).

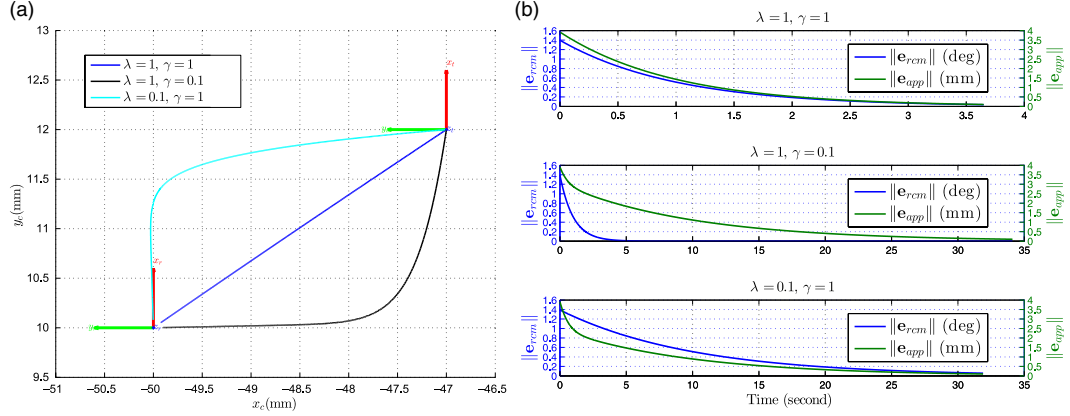
382 6.1. Outside phase: Control gain choice influence

383 A first test shows the influence of λ and γ for the first (40) and the second (45) tasks during the
 384 outside phase (46), as depicted in Fig. 12.

385 Throughout this first test, a straight tool was used during the various numerical trials where its
 386 tool tip frame \mathfrak{R}_t is located at the top right of Fig. 12(a), while the incision frame \mathfrak{R}_r is located at the
 387 bottom left.

388 The blue line, in Fig 12(a), represents the system behavior when $\lambda = 1$ and $\gamma = 1$. The system
 389 tends to reduce the alignment task error (40) faster than reducing the approach task error (45), if the
 390 value of λ is greater than γ (black line in Fig. 12(a)). In the opposite case, when γ is greater than λ ,
 391 the approach task converges faster than the alignment task (cyan line in Fig. 12(a)).

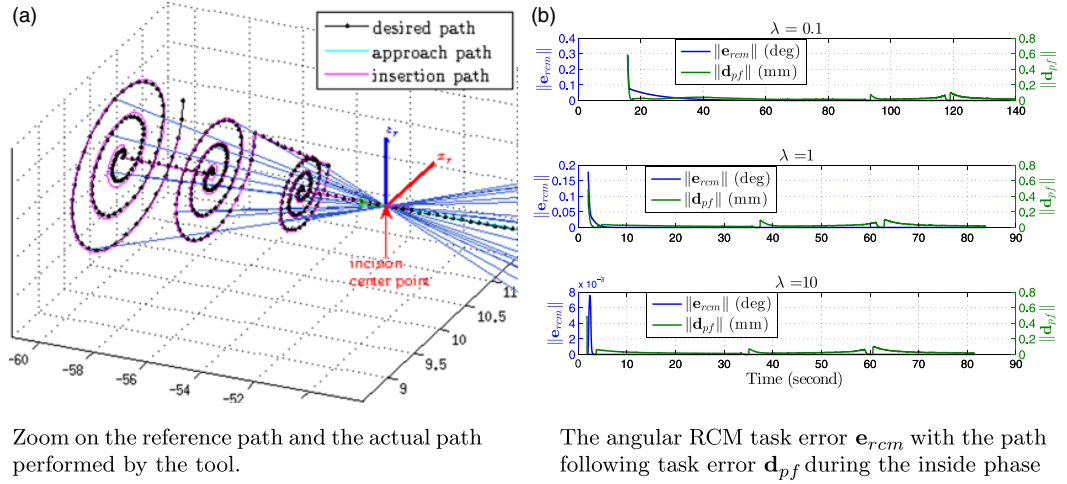
392 The evolution of the alignment task error and that of the approaching task are depicted in
 393 Fig. 12(b). It can be highlighted that for a faster exponential decay of these errors, one can increase
 394 the gain values.



Tool tip motion where the upper right corner is the initial position of the tool tip \mathfrak{R}_t and the lower left corner is the incision hole center point \mathfrak{R}_r .

Output errors of the alignment task \mathbf{e}_{rcm} and that of the approach task \mathbf{e}_{app} .

Fig. 12. The system performances during the outside phase while varying the values of λ and γ .



Zoom on the reference path and the actual path performed by the tool.

The angular RCM task error \mathbf{e}_{rcm} with the path following task error \mathbf{d}_{pf} during the inside phase

Fig. 13. Validation of the path-following task under the RCM constraint.

395 6.2. Inside phase: 3D path following under bilateral (RCM) constraints

396 This test simulates a driller (straight) tool in order to form a conical tunnel (i.e., incision hole). The
397 3D path is defined with respect to the incision frame \mathfrak{R}_r as depicted in Fig. 13(a), and it is composed
398 of (i) a linear portion along the basis r_y and its length is 13 mm and (ii) various steps of helical paths.

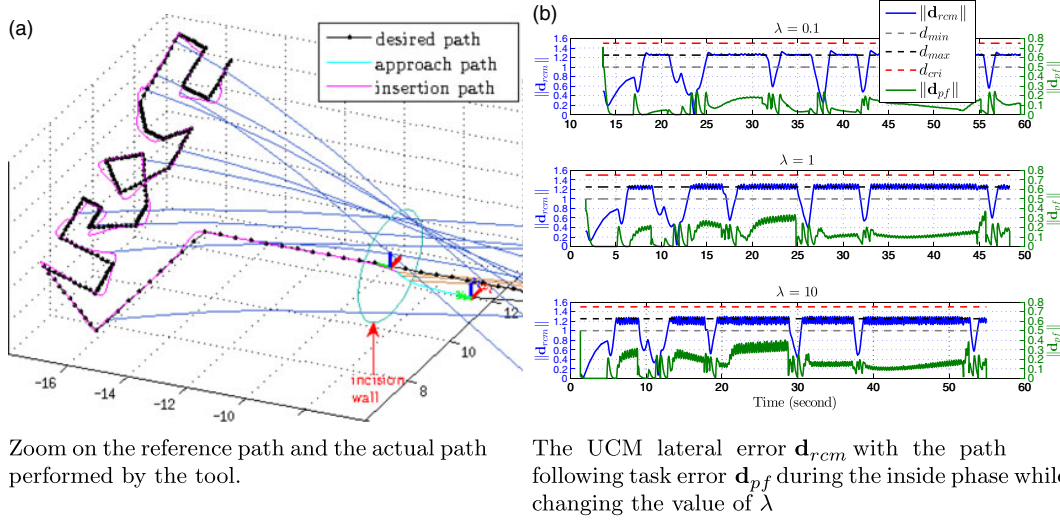
399 Throughout this phase, the task priority controller (47) arranges the alignment task as the highest
400 priority, while the second one is the path following ensured the incision task. Thereby, this test
401 focuses on the influence of the alignment gain λ , while the other gain values are constant, that is,
402 $v_{tis} = 2$ mm/s, $\beta = -3$, and $T_e = 0.01$ second (sampling period).

403 The system performances are shown in Fig. 13(b), where λ increases from 0.1, 1, to 10, for the
404 upper, middle, and lower plots, respectively. It can be highlighted that in the upper plot, the angular
405 alignment error \mathbf{e}_{rcm} is reduced exponentially as expected but it takes time to reduce and maintain it
406 at zero. However, the middle and lower plots show that the error \mathbf{e}_{rcm} reaches the zero quickly.

407 Besides that, one can observe that the task priority controller works well since the secondary (path
408 following) task error does not influence that of the first (alignment) one. The summary of the angular
409 error \mathbf{e}_{rcm} and that of the path following \mathbf{d}_{pf} during the different trials are presented in Table II, which
410 summarizes the median, the mean, and the standard deviation (STD) errors of both tasks (i.e., \mathbf{e}_{rcm}
411 and \mathbf{d}_{pf}).

Table II. Summary of different tests achieved with constant gain values (i.e., $v_{tis} = 2 \text{ mm/second}$ and $\beta = -3$) while the gain λ varies from 0.1 to 10.

λ	RCM angular error (deg)			PF error (mm)		
	Median	Mean	STD	Median	Mean	STD
0.1	0	0.007	0.018	0.022	0.027	0.023
1	0	0.001	0.011	0.022	0.027	0.02
10	0	0	0.001	0.022	0.027	0.016



Zoom on the reference path and the actual path performed by the tool.

The UCM lateral error \mathbf{d}_{rcm} with the path following task error \mathbf{d}_{pf} during the inside phase while changing the value of λ

Fig. 14. Validation of the path-following task under the UCM constraint.

6.3. Inside phase: 3D path following under the unilateral (UCM) constraints

This test validates the use of a curved tool (with circular portion shape) instead of the straight one. The achieved task consists of the following of a reference incision path under the UCM constraints. The reference path is defined by a linear portion and the word $\mu RoCS$, as depicted in Fig. 14(a). This figure also shows the incision wall represented by a dark green circle.

During this phase, the task priority controller chooses between (48) or (49) depending on the tool position with respect to the incision wall. Therefore, this simulated test shows the influence of alignment gain λ on the system performances (Fig. 14(b)), while the other gain values are constant (i.e., $v_{tis} = 2 \text{ mm/s}$, $\beta = -3$, and $T_e = 0.01 \text{ s}$). When the weighting factor λ is small, the lateral alignment error \mathbf{d}_{rcm} stays close to the border d_{max} with some overtaking (first plot in Fig. 14(b)). The values of d_{min} , d_{max} , and d_{cri} are constant during the different trials and then equal 1, 1.25, and 1.5 mm, respectively. However, if the value of λ is too big, the controller will provide high-velocity values. Consequently, the lateral alignment error \mathbf{d}_{rcm} slightly oscillates around the border d_{max} (third plot in Fig. 14(b)) but the system still stable.

Besides that, the reference path of this test is discontinuous. It is generally difficult to follow accurately a sharp path. Thus, the path-following error \mathbf{d}_{pf} is bigger compared to the previous test. However, the error \mathbf{d}_{pf} can be reduced by smoothing the sharp corners of the reference path (make them curvy) and/or modifying the path-following gains (v_{tis}/β).

Table III summaries the lateral alignment error \mathbf{d}_{rcm} and that of the path following \mathbf{d}_{pf} during the different trials.

7. Experimental Validation

This section deals with experimental validation of the different concepts and control methods proposed in this paper. This experimental validation was performed using a laboratory test bench as depicted in Fig. 15, which is composed, among other items, of a 3PPSR parallel robotic system of six degrees of freedom (dof). Each dof is actuated thanks to a high-resolution DC motor and

Table III. Summary of different tests achieved with constant gain values (i.e., $v_{is} = 2$ mm/s and $\beta = -3$), while the gain λ varies from 0.1 to 10.

λ	UCM lateral error (mm)			PF error (mm)		
	Median	Mean	STD	Median	Mean	STD
0.1	1.254	1.08	0.328	0.082	0.089	0.023
1	1.22	1.077	0.3	0.12	0.133	0.084
10	1.175	1.064	0.289	0.148	0.16	0.097

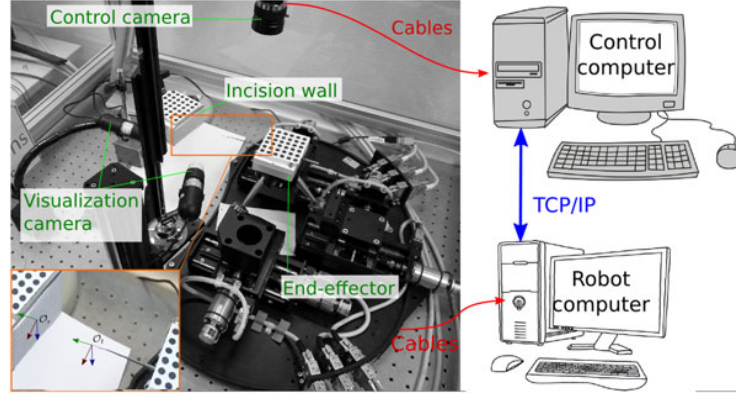


Fig. 15. Experimental setup configuration with a zoom on the tool tip and the incision wall.

437 high-accurate individual encoders. The robotic system is characterized with the following features^a
 438 : translation ranges $(t_x, t_y, t_z)_{max}^T = (50, 100, 12.7 \text{ mm})^T$, rotation ranges $(r_x, r_y, r_z)_{max}^T = (10^\circ, 10^\circ,$
 439 $10^\circ)^T$, a linear resolution of $0.2 \mu\text{m}$ (repeatability of $\pm 0.5 \mu\text{m}$), and an angular resolution of 0.0005°
 440 (repeatability of $\pm 0.0011^\circ$). The low level of robot control (i.e., inner PID loop, static, and differ-
 441 ential kinematic models) is done on a programmable logic controller, which communicates with a
 442 computer (a 2.33-GHz Xeon Intel CPU with a Windows distribution). Furthermore, the high-level
 443 control of the robot (i.e., task priority, both RCM and UCM, as well as the path-following controllers)
 444 is implemented on another computer (a 3.20-GHz i5 core Intel CPU with a Linux distribution), which
 445 sends the control velocities to the robot computer via TCP/IP protocol. The high-level computer is
 446 also used to communicate with a monocular camera for tracking and estimating the end-effector pose
 447 in real time (at the camera frame rate, i.e., 20 Hz).

448 Furthermore, the robot end effector carries a standard surgical tool (Fig. 16) that can be found
 449 actually in the operation room. It could be either a straight instrument (its diameter varies from 2.4
 450 mm at its base and 0.5 mm at its tip) or a curved one (formed by a portion of a circle where its radius
 451 is around 16 mm and its diameter is 1 mm). Besides that, the incision wall is represented by a sheet
 452 of paper which acts as a fragile membrane. It is used to demonstrate that the tool does not tear the
 453 paper while following the desired path under the RCM or UCM tasks.

454 7.1. Implementation details

455 The proposed controller was implemented in C++ by using ViSP (Visual Servoing Platform)
 456 library.²⁷ The code is divided into C++ classes which are summarized in Algorithm 1.

457 The user (e.g., a surgeon and/or operator) starts by defining the reference path before the control
 458 loop begins (offline). The geometric curve is generally determined during the per-operative phase
 459 where a planning software deduces the optimal path²⁸⁻³⁰ or the surgeon draws the curve on a tactile
 460 tablet^{b, 31-33}

^aThe data sheet of the PI parallel robot *SpaceFAB SF-3000 BS* is available online <https://www.physikinstrumente.com/en/products/parallel-kinematic-hexapods/hexapods-with-motor-screw-drives/sf-3000-bs-spacefab-1204400/>

^b μ RALP (Micro-technologies and Systems for Robot-Assisted Laser Phonomicrosurgery). [online] <http://www.microralp.eu/>

Algorithm 1 Summarizing the controller code.

Result: robot velocity twist vector (${}^e\mathbf{v}_e$)
parameter: initialize model parameters ($\lambda, \gamma, v_{tis}, \beta$)
Data: reference path ($\mathcal{S}_p(s_p)$)
 $({}^e\mathbf{M}_t, {}^c\mathbf{M}_w, {}^c\mathbf{M}_r, {}^c\mathbf{M}_e) \leftarrow$ initialize homogeneous matrices (image)
while (! task accomplished) **do**
 if PATH FOLLOWED == 1 *or* INTER == MAX **then**
 | **task accomplished**
 else
 | $({}^c\mathbf{M}_e, {}^c\mathbf{M}_r) \leftarrow$ features tracking (image)
 | $(\mathbf{e}_{rcm}, \mathbf{d}_{rcm}) \leftarrow$ compute RCM/UCM variables (${}^e\mathbf{u}_{er}, {}^e\mathbf{u}_{et}, {}^e\mathbf{et}$)
 | $\mathbf{L}_{e_{rcm}} \leftarrow$ alignment task (λ)
 | **if** CHECK PHASE **then**
 | | **outside phase**
 | | $\mathbf{L}_{e_{app}} \leftarrow$ point regulation (γ)
 | | **else**
 | | **path following task**
 | | $\mathbf{d}_{pf} \leftarrow$ tool tip projection on the path (${}^c\mathbf{M}_e, {}^e\mathbf{M}_t, \mathcal{S}_p(s_p)$)
 | | $(\mathbf{L}_{e_{pf}}, \mathbf{v}_t) \leftarrow$ compute tool tip linear velocity (v_{tis}, β)
 | | **if** END OF PATH **then**
 | | | PATH PERFORMED \leftarrow 1
 | | **end**
 | | **end**
 | | **arrange task priority**
 | | ${}^e\mathbf{v}_e \leftarrow$ projection of the 2nd task into the null-space of the 1st task
 | | **send the velocity to the robot** (${}^e\mathbf{v}_e$)
 | **end**
end
end



Fig. 16. The different surgical tools used during the experimental validation.

461 Afterward, the user initializes the parameters of each controller depending on the task to be per-
 462 formed. Thus, the control loop starts by updating the different homogeneous matrices representing
 463 the pose (position and rotation) of the various frames. Thereafter, the control velocity for maintaining
 464 the RCM/UCM task is then computed (40) or (42). Then, the control velocity of the second task is
 465 computed to converge toward the trocar point (45) or to follow the desired path (3).

466 Finally, the task priority controller manages the hierarchical priority between tasks as depicted in
 467 Section 5.2.

468 7.2. Results: 3D path following under bilateral (RCM) constraints

469 This test evaluates the proposed controller while using a straight tool for following a spiral path.
 470 Fig. 17(a) shows the general motion of the tool tip during the inside phase, while Fig. 17(b) presents

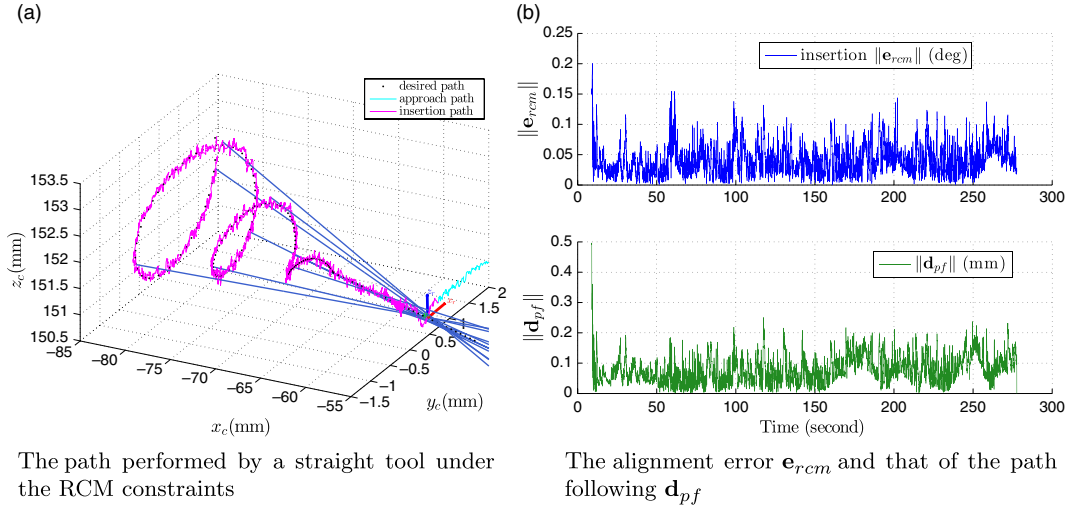


Fig. 17. The results obtained from the parallel robot, during the inside phase, while using a straight tool under RCM constraints.

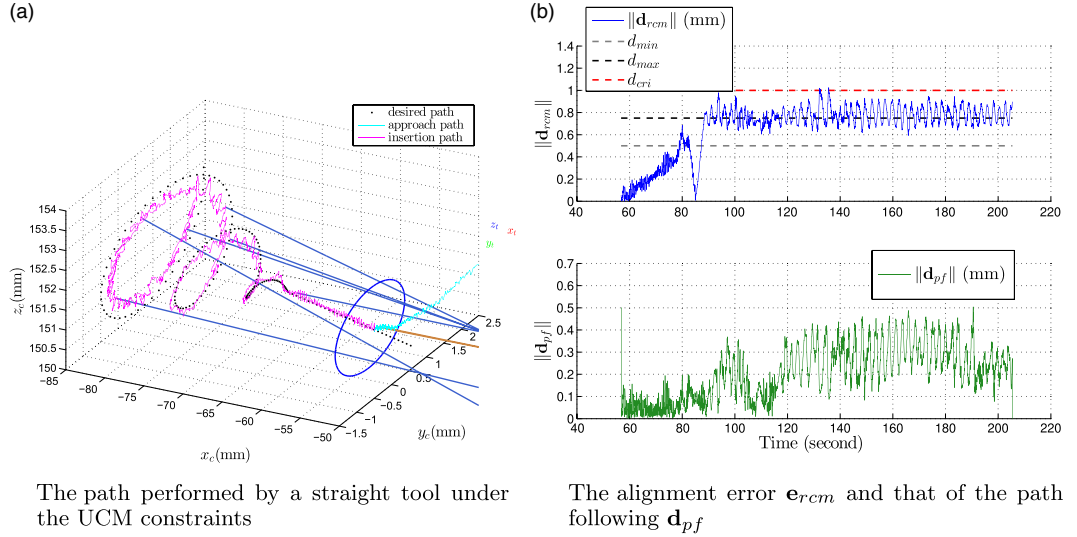


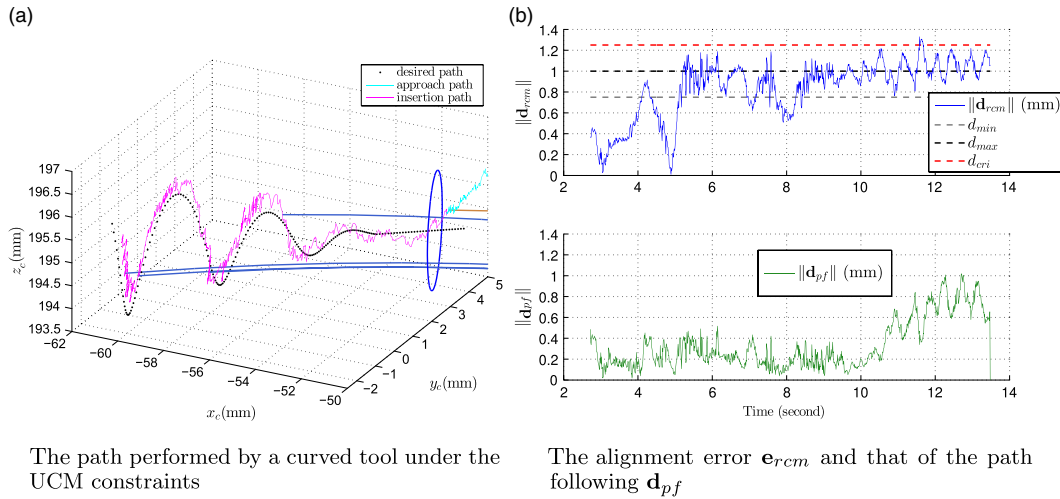
Fig. 18. The results obtained from the parallel robot while using a straight tool.

471 the system performances. As expected, the alignment error \mathbf{e}_{rcm} maintains its value around zero, as
 472 depicted in the upper plot in Fig. 17(b). The error \mathbf{e}_{rcm} was measured during the inside phase to be
 473 $0.04^\circ \pm 0.02^\circ$ (i.e., mean error \pm STD error) and its median error was 0.035° .

474 The lower plot of Fig. 17(b) shows the evolution of the path following \mathbf{d}_{pf} . It was measured
 475 as 0.08 ± 0.05 mm, and its median error was 0.068 mm during the inside phase. The gain values
 476 used during this validation tests are fixed as follows: $\lambda = 0.8$, $\gamma = 1$, $v_{tis} = 4$ mm/s, $\beta = -8$, and
 477 $T_e = 0.05$ s.

478 7.3. Results: 3D path following under unilateral (UCM) constraints

479 **Straight tool.** This test deals with the validation of the proposed controller under a UCM constraint
 480 while using a straight tool. The reference path was chosen as a spiral curve with its maximum radius
 481 reaches 2 mm. Figure 18(a) shows the tool motion through the incision hole, where the boundary
 482 d_{cri} is represented by circle. Also, Fig. 18(b) shows the evolution of the positioning errors during
 483 the tool motion. As expected, the lateral alignment error \mathbf{d}_{rcm} was limited between the boundaries
 484 $d_{min} = 0.5$, $d_{max} = 0.75$ and $d_{cri} = 1$ mm. Indeed, the \mathbf{d}_{rcm} error was measured during the inside phase



The path performed by a curved tool under the UCM constraints

The alignment error \mathbf{e}_{rcm} and that of the path following \mathbf{d}_{pf}

Fig. 19. The results obtained from the parallel robot while using a curved tool.

485 to be $0.67 \pm 0.23\text{mm}$ and its median value as 0.73 mm . Besides that, the path-following error \mathbf{d}_{pf} was
 486 measured to be $0.208 \pm 0.12\text{ mm}$ and its corresponding median value 0.207 mm . In fact, the lateral
 487 alignment error is coupled with the path following, as shown in Fig. 18(b) near the time 120 s , the
 488 slight oscillations of \mathbf{d}_{rcm} error around the boundary d_{max} cause the \mathbf{d}_{pf} to oscillate also. These results
 489 are produced with the following control gains: $\lambda = 0.8$, $v_{vis} = 2\text{ mm/s}$, $\beta = -4$, and $T_e = 0.05\text{ s}$.

490 *Curved tool:* In the second test, the straight tool was replaced by a curved one and the output results
 491 are presented in Fig. 19(a). The reference path is the same as the previous test, but it is rotated about
 492 the z-axis. Fig. 19(b) shows the system performances during the inside phase. The lateral alignment
 493 error \mathbf{d}_{rcm} was measured as $0.83 \pm 0.28\text{ mm}$ and its median value was 0.92 mm . The \mathbf{d}_{rcm} error is
 494 bigger compared to the previous test due to the gain $\lambda = 0.5$ is smaller than the previous test. A bigger
 495 value of λ generates poses that are not reachable with the parallel robot since the robot reaches its
 496 workspace limit. Moreover, the path-following error \mathbf{d}_{pf} was measured to be $0.33 \pm 0.24\text{ mm}$ and
 497 its median value was 0.24 mm . These results are produced with the following control gains values:
 498 $v_{vis} = 2\text{ mm/s}$, $\beta = -3$, and $T_e = 0.01\text{ s}$.

499 8. Conclusion and Perspectives

500 This article demonstrated the proof of concept of a control scheme for constrained motions as
 501 RCM and UCM while using either straight-line or fixed-curve surgical tools. The proposed methods
 502 offer a generic formulation of the constrained motion problem with high flexibility, which means
 503 easy/intuitive integration in various systems or purposes since RCM and UCM constraints were
 504 described in the task space. In fact, this methodology does not require precise knowledge of the
 505 robot inverse kinematics.

506 Another ‘‘surgical’’ task was included in the problem formulation as a path-following scheme
 507 mimicking excision/ablation clinical interventions. Indeed, the surgeon can draw a predefined exci-
 508 sion path using preoperative images that the tool must achieve under the constrained motion (RCM
 509 or UCM). A task-prioritizing paradigm was developed to manage the performing of two or more
 510 tasks without conflicts. Thereafter, the proposed methods were successfully validated (under various
 511 scenarios) both numerically using a developed simulator and experimentally using a 6-DoF robotic
 512 setup.

513 Finally, it would be valuable for the perspectives to investigate what is the optimal geometric form
 514 of the curved tool in order to achieve a maximum displacement while minimizing the collision risk
 515 with anatomical structures. Besides that, the proposed controller will be evaluated in *in vitro* and *ex*
 516 *vivo* experiments. Furthermore, the controller can be extended to include the robot dynamics (i.e., a
 517 force controller). Integrating a flexible tool will as well increase the dexterity and the maneuverability
 518 of the distal tool tip.

519 **References**

- 520 1. T. Osa, C. Staub and A. Knoll, "Framework of Automatic Robot Surgery System Using Visual Servoing,"
521 **In: IEEE/RSJ International Conference on Intelligent Robots and Systems** (2010) pp. 1837–1842. **Q5**
- 522 2. M. M. Dalvand and B. Shirinzadeh, "Remote Centre-of-Motion Control Algorithms of 6-RRCCR Parallel
523 Robot Assisted Surgery System (PRAMiSS)," **In: IEEE International Conference on Robotics and
524 Automation** (2012) pp. 3401–3406.
- 525 3. I. Fleming, M. Balicki, J. Koo, et al., "Cooperative Robot Assistant for Retinal Microsurgery," **In:
526 International Conference on Medical Image Computing and Computer-Assisted Intervention** (Springer,
527 2008) pp. 543–550.
- 528 4. Y. Ida, N. Sugita, T. Ueta, et al., "Microsurgical robotic system for vitreoretinal surgery," *Int. J. Comput.*
529 *Assist. Radiol. Surgery* **7**(1), 27–34 (2012). **Q6**
- 530 5. R. H. Taylor, J. Funda, D. D. Grossman, et al., "Remote Center-of-Motion Robot for Surgery," (1995), US
531 Patent 5,397,323.
- 532 6. B. Dahroug, B. Tamadazte and N. Andreff, "Task Controller for Performing Remote Centre of Motion,"
533 **In: Lecture Note on Electrical Engineering**. Springer (2017).
- 534 7. A. Blumentals, B. Brogliato and F. Bertails-Descoubes, "The contact problem in Lagrangian systems sub-
535 ject to bilateral and unilateral constraints, with or without sliding Coulombs friction: A tutorial," *Multibody
536 Syst. Dyn.* **38**(1), 43–76 (2016). **Q7**
- 537 8. P. J. Swaney, J. M. Croom, J. Burgner, et al., "Design of a Quadramanual Robot for Single-Nostril Skull
538 Base Surgery," **In: ASME Annual Dynamic Systems and Control Conference**, vol. 3 (American Society of
539 Mechanical Engineers, 2012) pp. 387–393.
- 540 9. C. Girerd, K. Rabenorosoa and P. Renaud, "Combining Tube Design and Simple Kinematic Strategy for
541 Follow-the-Leader Deployment of Concentric Tube Robots," **In: Advances in Robot Kinematics** (2016)
542 pp. 23–31.
- 543 10. M. Miroir, Y. Nguyen, J. Szewczyk, et al., "Robotol: From design to evaluation of a robot for middle ear
544 surgery," **In: IEEE/RSJ International Conference on Intelligent Robots and Systems** (2010), pp. 850–856.
- 545 11. K. Entsfellner, R. Tauber, D. B. Roppenecker, et al., "Development of universal gripping adapters: Sterile
546 coupling of medical devices and robots using robotic fingers," **In: IEEE/ASME International Conference
547 on Advanced Intelligent Mechatronics** (2013) pp. 1464–1469.
- 548 12. B. Dahroug, B. Tamadazte, B. Weber, et al. "Review on otological robotic systems: Toward microrobot-
549 assisted cholesteatoma surgery," *IEEE Rev. Biomed. Eng.* **11**, 125–142 (2018).
- 550 13. Y. Nakamura, H. Hanafusa and T. Yoshikawa, "Task-priority based redundancy control of robot manipula-
551 tors," *Int. J. Robot. Res.* **6**(2), 3–15 (1987). **Q8**
- 552 14. B. Siciliano, "Kinematic control of redundant robot manipulators: A tutorial," *J. Intel. Robot. Syst.* **3**,
553 201–212 (1990).
- 554 15. N. Mansard and O. Khatib, "Continuous Control Law from Unilateral Constraints," *IEEE International
555 Conference on Robotics and Automation* (2008) pp. 3359–3364.
- 556 16. C.-H. Kuo, J. S. Dai and P. Dasgupta, "Kinematic design considerations for minimally invasive surgical
557 robots: An overview," *Int. J. Med. Robot. Comput. Assist. Surg.* **8**(2), 127–145 (2012).
- 558 17. J. Funda, R. H. Taylor, B. Eldridge, et al., "Constrained cartesian motion control for teleoperated surgical
559 robots," *IEEE Trans. Robot. Autom.* **12**, 453–465 (1996).
- 560 18. H. Azimian, R. V. Patel, and M. D. Naish, "On Constrained Manipulation in Robotics-Assisted
561 Minimally Invasive Surgery," **In: IEEE RAS/EMBS International Conference on Biomedical Robotics and
562 Biomechatronics** (2010) pp. 650–655.
- 563 19. M. M. Marinho, M. C. Bernardes and A. P. Bó, "A Programmable Remote Center-of-Motion Controller for
564 Minimally Invasive Surgery Using the Dual Quaternion Framework," **In: IEEE RAS & EMBS International
565 Conference on Biomedical Robotics and Biomechatronics** (2014) pp. 339–344.
- 566 20. C. D. Pham, F. Coutinho, A. C. Leite, et al., "Analysis of a Moving Remote Center of Motion for Robotics-
567 Assisted Minimally Invasive Surgery," **In: IEEE/RSJ International Conference on Intelligent Robots and
568 Systems** (2015) pp. 1440–1446.
- 569 21. H. Mayer, I. Nagy and A. Knoll, "Kinematics and Modelling of a System for Robotic Surgery," **In:
570 Advances in Robot Kinematics** (2004), pp. 181–190.
- 571 22. E. M. Boctor, R. J. Webster III, H. Mathieu, et al., "Virtual remote center of motion control for needle
572 placement robots," *Comput. Aid. Surg.* **9**, 175–183 (2004).
- 573 23. B. Dahroug, J. A. Seon, A. Oulmas, T. Xu, B. Tamadazte, et al., "Some Examples of Path Following in
574 Microrobotics," **In: IEEE International Conference on Manipulation, Automation and Robotics at Small
575 Scales** (2018) pp. 1–6.
- 576 24. L. B. Rosenberg, "Virtual Fixtures: Perceptual Tools for Telerobotic Manipulation," **In: IEEE Virtual
577 Reality Annual International Symposium** (1993) pp. 76–82.
- 578 25. S. A. Bowyer, B. L. Davies and F. R. y Baena, "Active constraints/virtual fixtures: A survey," *IEEE Trans.
579 Robot.* **30**(1), 138–157 (2014).
- 580 26. B. Dahroug, B. Tamadazte and N. Andreff, "Visual Servoing Controller for Time-Invariant 3D Path
581 Following with Remote Centre of Motion Constraint," **In: IEEE International Conference on Robotics
582 and Automation** (2017) pp. 3612–3618.
- 583 27. E. Marchand, F. Spindler and F. Chaumette, "Visp for Visual Servoing: A Generic Software Platform with
584 a Wide Class of Robot Control Skills," *IEEE Robot. Autom. Mag.* **12**, 40–52 (2005).

- 585 28. M. Kazemi, K. Gupta and M. Mehrandezh, "Path-Planning for Visual Servoing: A Review and Issues," **In:**
586 *Visual Servoing via Advanced Numerical Methods*. Springer, 2010, pp. 189–207.
- 587 29. N. Gerber, B. Bell, K. Gavaghan, et al., "Surgical planning tool for robotically assisted hearing aid
588 implantation," *Int. J. Comput. Assist. Radio. Surg.* **9**(1), 11–20 (2014).
- 589 30. A. Gasparetto, P. Boscariol, A. Lanzutti and R. Vidoni, "Path Planning and Trajectory Planning Algorithms:
590 A General Overview," **In:** *Motion and Operation Planning of Robotic Systems*. Springer (2015), 3–27.
- 591 31. J. A. Seon, B. Tamadazte and N. Andreff, "Decoupling path following and velocity profile in vision-guided
592 laser steering," *IEEE Trans. Robot.* **31**(2), 280–289 (2015).
- 593 32. R. Renevier, B. Tamadazte, K. Rabenorosoa, et al., "Endoscopic laser surgery: Design, modeling, and
594 control," *IEEE/ASME Trans. Mechatron.* **22**(1), 99–106 (2017).
- 595 33. B. Tamadazte, R. Renevier, J. Séon, et al., "Laser beam steering along three-dimensional paths,"
596 *IEEE/ASME Trans. Mechatron.* **23**(3), 1148–1158 (2018).